Research Article | Vol. 31, No. 4 / 13 Feb 2023 / Optics Express 5334

Optics EXPRESS

# General mathematical model for the period chirp in interference lithography

FLORIAN BIENERT,* THOMAS GRAF, AND MARWAN ABDOU AHMED

*Universität Stuttgart, Institut für Strahlwerkzeuge (IFSW), Pfaffenwaldring 43, 70569 Stuttgart, Germany*
*florian.bienert@ifsw.uni-stuttgart.de

**Abstract:** We present a general analytical model for the calculation of the spatial distribution of the grating period, enabling the unification of all configurations of classical laser interference lithography (LIL) and scanning-beam interference lithography (SBIL) into one formalism. This is possible due to the consideration of Gaussian beams instead of point sources which allow for the accurate description of not only the laser's far-field but also its near-field. The proposed model enables the calculation of the grating period, the inclination and the slant of the grating lines on arbitrarily shaped substrates, originating from the interference of arbitrarily orientated and positioned Gaussian beams.

Published by Optica Publishing Group under the terms of the Creative Commons Attribution 4.0 License. Further distribution of this work must maintain attribution to the author(s) and the published article's title, journal citation, and DOI.

## 1. Introduction

Interference lithography (IFL) is a common technique used for the generation of small periodic structures. Depending on the arrangement and the number of interfering beams, various patterns can be created. The most common variant comprising two interfering laser beams is especially suited for the exposure of linear holographic gratings. Their wide range of applications includes chirped pulse amplification (CPA) [1–3], spectroscopy [4], and polarization selection or transformation [5–7], and their use as intracavity elements in laser oscillators [8–12] drives the development of IFL and underline its importance. Two-beam IFL is mainly distinguished into two types. The classical laser interference lithography (LIL) [13,14] employs the exposure of the photo-resists using the laser's far-field, as shown by the simplified sketch in Fig. 1(a). A diffraction-limited spectrally narrow-banded laser beam is split up and its replicas are focused through apertures and interfere on the substrate at an angle $\theta$. The intrinsic non-planarity of the laser's wavefronts however creates an interference pattern exhibiting a spatial dependence of the period, known as period chirp. This detrimental effect was already observed in 1977 [15] and has been addressed in various publications [16–22]. To avoid the problems arising with the period chirp and to allow for the patterning of larger substrates (up to one meter), a more recent technique called scanning beam interference lithography (SBIL) was developed at the MIT by Chen. et al. [23,24]. SBIL is based on the interference of the beams in the near-field, i.e. at their waist where the wavefronts are plane. This is schematically shown in Fig. 1(b). Since the area of the interference pattern is however much smaller than the one in LIL, the technique relies on the scanning of the interference pattern over the substrate [25]. Although the period chirp can widely be eliminated with SBIL, it can still occur here. Reasons might be focus shifts and wavy substrates but it can also appear with perfect alignment due to poor choice of collimation and laser parameters. This is because the wavefronts are only exactly plane at the beam's waist and thus at one point on the substrate (see green point in the insert of Fig. 1(b)). With deviating positions from this point (see orange point), the wavefront's curvature increases up to a maximum curvature at a distance of one Rayleigh length.

#481887
Journal © 2023

https://doi.org/10.1364/OE.481887
Received 25 Nov 2022; accepted 11 Jan 2023; published 30 Jan 2023

Optics EXPRESS

**Fig. 1.** Schematic representation of classical laser interference lithography (LIL) [21] (a), of scanning beam interference lithography (SBIL) (b), where the insert shows the beams and the curvature of their wavefronts at the waist, and of the unified model for Gaussian beams (c), allowing for the description of both LIL and SBIL.

Various models and equations have been developed for the classical LIL to allow for the calculation of the spatial distribution of the period in order to determine the period chirp [16–20]. All these models are based on the assumption, that the two laser beams can be described by spherical waves, originating from two point sources, cf. point A and B in Fig. 1(a). This assumption eases the modelling and the mathematical description is valid since the interference pattern is created in the far-field of the beam. These point source models however need to be adapted for different setups, depending on whether interference between convex, concave, or convex and concave wavefronts is considered [20]. For SBIL, where the inference is created in the beam's near-field, cf. Figure 1(b), the point source assumption cannot be used. The spatial dependence of the wavefront's curvature makes the modelling and determination of the wavefront vector more complex and to the best of our knowledge, no model for the description of the period chirp – or the spatial distribution of the period– has ever been presented for SBIL yet.

The goal of this publication is therefore to provide a general model, covering both LIL and SBIL. Case distinctions are no longer necessary with this unified model and it is no more restricted to the laser's near-field or far-field. We derive the description of the interference between two arbitrarily positioned and arbitrarily orientated Gaussian beams on an arbitrarily shaped and arbitrarily orientated substrate, cf. Figure 1(c). The model focuses on the calculation of the obtained grating period, as well as the inclination and the slant of the grating lines.

## 2. Modeling

Three objects need to be considered in the proposed model: the two Gaussian beams, $G_A$ and $G_B$, and the substrate's surface $S$, as shown in Fig. 2(a). All objects are defined at arbitrary positions and with arbitrary orientations in a superior coordinate system. Each of the beams is defined by a positional vector $\vec{\boldsymbol{h}}$ describing the waist position with respect to the origin $O$ of the superior coordinate system, a directional vector $\vec{\boldsymbol{a}}$ indicating the propagation direction on the axis of the beam, the radius $w_{00}$ of the waist, the Rayleigh length $z_R$, and the wavelength $\lambda$. In Fig. 2(a) these parameters are highlighted on the example of the Gaussian beam $G_A$ (red). The beams are assumed to be symmetric. For their description of their electric field

$$E_{00}(r,z,t) = E_0 \frac{z_R}{\sqrt{z^2 + z_R^2}} \cdot e^{-\frac{r^2}{w_{00}^2(z)}} \cdot e^{-\frac{ikr^2}{2R(z)}} \cdot e^{-i(kz-\omega t)} \cdot e^{i \cdot \arctan\left(\frac{z}{z_R}\right)} \tag{1}$$

we use the formalism for paraxial beams [26], where $z$ and $r$ are the local coordinates along and perpendicular to the beam's optical axes, $E_0$ is the amplitude at the origin $z = r = 0$, $R$ the wavefront's radius of curvature, $k$ the wave number, and $\omega$ the angular frequency.

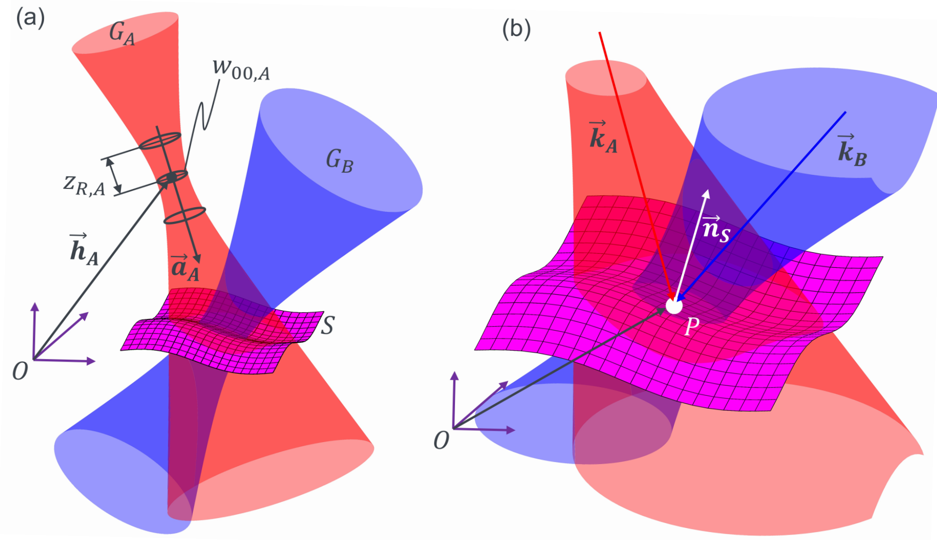


**Fig. 2.** Arrangement of the objects considered in the proposed model. The interference between two arbitrarily defined, positioned, and orientated Gaussian beams on an arbitrarily shaped substrate is considered. (a): Parameters used for the description of the Gaussian beam, exemplarily shown on beam $G_A$. (b): Parameters of the substrate at a defined point $P$.

The surface $S$ is defined by an arbitrary function whereby each point $P$ in it is described by its position and a normal vector $\vec{n}_S$, being perpendicular to the surface at the point $P$. This is shown at an exemplary point in Fig. 2(b).

The derivation of the equations for the determination of the grating parameters is divided into two steps. The first, described in section 2.1, is the determination of the wavefront vectors $\vec{k}_A$ and $\vec{k}_B$ of the two beams at a given point $P$ on the substrate $S$. The second step, which is discussed in section 2.2, is the determination of the grating parameters that results from the interference of the two wavefronts near the point $P$.

### 2.1. Determination of the wavefront vectors

To begin, a plane is defined, incorporating the point $P$ and the axis of the Gaussian beam. This plane is shown in Fig. 3, including the caustic of the beam and its local coordinate system given by the coordinates $z$ and $r$, together with several additional points which are required for the derivation. The point $P$ is located on the spherical wavefront $W$ (orange). The center of the wavefront $W$ is located at the point $Q$. In the depicted situation the wavefront vector $\vec{k}_A$ (red) of the wave incident at the point $P$ is therefore parallel to the vector $\overrightarrow{QP}$ (green). If the point $P$ is however located in front of the beam's waist (see insert with $P^*$) the wavefront vector $\vec{k}_A$ is anti-parallel to $\overrightarrow{QP}$. Respecting these two cases the wavefront vector $\vec{k}_A$ can be defined as

$$\vec{k}_A = \frac{\overrightarrow{QP}}{|\overrightarrow{QP}|} \cdot k_A \cdot \frac{z_A}{|z_A|} \tag{2}$$

Optics EXPRESS

where $k_A$ is the wave number and the last term of Eq. (2) defines the correct sign of the wavefront vector. The value $z_A$ thereby describes the distance between the intersection of the wavefront $W$ with the beam's optical axis and the point $A$ at the waist of the beam. The point $Q$ is located on the beam's optical axis at a distance $z_Q$ from the point $A$. With the origin of the global coordinate system $O$, the point $Q$ can be described as

$$\overrightarrow{OQ} = \overrightarrow{OA} + \frac{\vec{\boldsymbol{a}}_A}{|\vec{\boldsymbol{a}}_A|} \cdot z_Q. \tag{3}$$

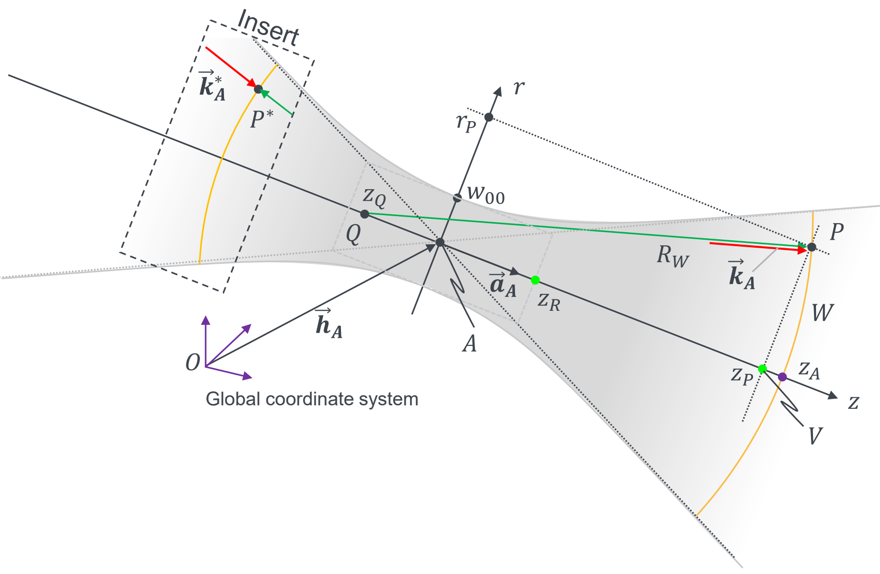


**Fig. 3.** Cross-section of the caustic of the Gaussian beam $G_A$ showing the parameters required for the derivation of the wavefront vector $\vec{\boldsymbol{k}}_A$ at the point $P$.

The value of $z_Q$ can be determined using the beam's local coordinate system, where it is given by

$$z_Q = z_A - R_W \tag{4}$$

with $R_W$ being the radius of curvature of the wavefront $W$. This curvature in turn is given by

$$R_W = z_R \left( \frac{z_A}{z_R} + \frac{z_R}{z_A} \right). \tag{5}$$

Furthermore, it can be stated that

$$R_W^2 = (z_P - z_Q)^2 + r_P^2 \tag{6}$$

where the values $z_P$ and $r_p$ are the coordinates of the point $P$ in the beam's local coordinate system. By inserting Eq. (5) into (6) one finds

$$z_R^2 \left( \frac{z_A}{z_R} + \frac{z_R}{z_A} \right)^2 = \left( z_P - z_A + z_R \left( \frac{z_A}{z_R} + \frac{z_R}{z_A} \right) \right)^2 + r_P^2. \tag{7}$$

Optics EXPRESS

Solving this for $z_A$ (e.g. using a symbolic solver) yields

$$z_A(r_P, z_P, z_R) = \frac{\left(54z_R^2 \cdot z_P + \sqrt{(2916 \cdot z_R^4 \cdot z_P^2 + 4(6z_R^2 - 3r_P^2 - 3z_P^2)^3)}\right)^{\frac{1}{3}}}{3 \cdot 2^{\frac{1}{3}}} - \frac{2^{\frac{1}{3}}(6z_R^2 - 3r_P^2 - 3z_P^2)}{3\left(54z_R^2 \cdot z_P + \sqrt{(2916 \cdot z_R^4 \cdot z_P^2 + 4(6z_R^2 - 3r_P^2 - 3z_P^2)^3)}\right)^{\frac{1}{3}}}. \tag{8}$$

In order to derive the local coordinates $z_P$ and $r_p$ from the global coordinates of the point $P$ we project $P$ onto the beam's optical axis, leading to the point $V$ given by [32]

$$\overrightarrow{OV} = \overrightarrow{OA} + \frac{\overrightarrow{PA} \cdot \vec{\boldsymbol{a}}_{\boldsymbol{A}}}{|\vec{\boldsymbol{a}}_{\boldsymbol{A}}|^2} \cdot \vec{\boldsymbol{a}}_{\boldsymbol{A}}. \tag{9}$$

The distance $z_P$ is then given by

$$z_P = |\overrightarrow{AV}| \cdot \frac{\vec{\boldsymbol{a}}_{\boldsymbol{A}} \cdot \overrightarrow{AV}}{|\vec{\boldsymbol{a}}_{\boldsymbol{A}}| \cdot |\overrightarrow{AV}|} \tag{10}$$

where the first term determines the length and the second term is used to define the correct sign, depending on whether the point $P$ is located in front or behind the beam's waist. Due to the beam's rotational symmetry the value $r_p$ can be defined without sign distinction and is thus given as

$$r_P = |\overrightarrow{PV}|. \tag{11}$$

The wave number $k_A$ being the length of the wavefront vector $\vec{\boldsymbol{k}}_{\boldsymbol{A}}$ depends on the wavelength of the beam. The gouy phase however leads to an effective change of the wave number and thus also of the wavelength [27] near the beam's waist, making $k_A$ a spatially dependent quantity. From Eq. (1) the phase $\varphi(z)$ on the axis of a Gaussian beam at a given time $t$ is given by

$$\varphi(z, z_R, \lambda) = \frac{2\pi}{\lambda} z - \arctan\left(\frac{z}{z_R}\right) - \omega t + \phi_0 \tag{12}$$

where $\phi_0$ is an arbitrary phase shift. The wave number at the location $z = z_A$ can be defined by the derivative of Eq. (12) resulting in

$$k_A(z = z_A) = |\vec{\boldsymbol{k}}_{\boldsymbol{A}}| = \frac{d\varphi(z = z_A, z_R, \lambda)}{dz} = \frac{2\pi}{\lambda_0} - \left(\frac{z_A^2}{z_R} + z_R\right)^{-1} \tag{13}$$

### *2.2. Determination of the grating properties*

In this section we derive the period, the inclination and the slant of the grating lines. These three parameters arise from the intersections between the substrate and the so-called planes of constructive interference (POCIs) [20]. They result from the interference of two Gaussian beams as introduced above. The physical meanings of the three grating parameters are shown in Fig. 4.

The grating period $\Lambda$ is the distance between two grating lines as shown in Fig. 4(a). It is typically described by a scalar $\Lambda$, but may be expressed as a vector $\vec{\boldsymbol{\Lambda}}$ to additionally convey the orientation of the lines. The spatially varying inclination of the grating lines, i.e. their bending, is coupled to the period chirp. This property is best analyzed with the help of the vectors $\vec{\boldsymbol{g}}$ given by the tangents to the grating lines. With reference to another vector (typically the grating vector

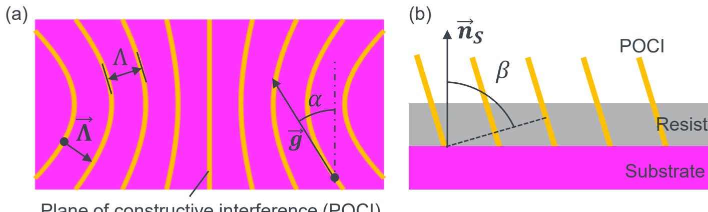


**Fig. 4.** (a): Top view of the grating lines on a substrate illustrating the physical meanings of the grating period $\Lambda$ and the inclination $\alpha$ of the grating lines. The inclination is defined by the angle between the tangential vector $\vec{\boldsymbol{g}}$ and another line, e.g., the dash-dotted line which represents the vector $\vec{\boldsymbol{g}}$ for the un-chirped case. (b): Front view of grating lines on a substrate illustrating the physical meaning of the slant $\beta$ of the grating lines, originating from the tilted exposure of the resist. The slant is defined by the angle β between the normal vector of the POCI and the normal vector of the substrate.

for the un-chirped case), it can be transformed into an angle describing the local inclination of the grating line, cf. $\alpha$ in Fig. 4(a). The third parameter, the slant of the grating lines, is shown in Fig. 4(b). The tilt of POCIs results in a slanted exposure of the resist. Depending on the subsequent etching processes this tilt is transferred to the grating lines [28]. The slant is defined by the angle $\beta$ between the normal of the tangential plane to interference pattern and the normal vector of the substrate. This parameter is especially important for the exposure of tilted and curved substrates [21,22,29].

The calculation is started by considering the tangential plane (magenta) to the substrate's surface at the point $P$ as illustrated in Fig. 5. This tangential plane is specified by the normal vector $\vec{\boldsymbol{n}}_S$ as schematically shown in Fig. 5(c) and (d). In a local approximation very close to the point $P$ the incident wavefronts of the two beams $G_A$ (red) and $G_B$ (blue) may also considered to be plane and specified by the local wavefront vectors $\vec{\boldsymbol{k}}_{\boldsymbol{A}}$ and $\vec{\boldsymbol{k}}_{\boldsymbol{B}}$. The wavefronts are moving in the direction of the wavefront vectors with time $t$, creating the POCIs which are constant in time. As already introduced in Fig. 4, the POCIs are schematically illustrated by the orange planes. The determination of their orientation and periodicity occurs by considering the illustration in Fig. 5(b) where the drawing plane is the plane which is spanned by the wavefront vectors $\vec{\boldsymbol{k}}_{\boldsymbol{A}}$ and $\vec{\boldsymbol{k}}_{\boldsymbol{B}}$. The wave vector of the periodic POCIs is given by

$$\vec{\boldsymbol{k}}_{\boldsymbol{I}} = \vec{\boldsymbol{k}}_{\boldsymbol{A}} - \vec{\boldsymbol{k}}_{\boldsymbol{B}}. \tag{14}$$

The distance between adjacent POCIs is then given by

$$\Lambda_I = \frac{2\pi}{|\vec{\boldsymbol{k}}_{\boldsymbol{I}}|}. \tag{15}$$

The three exemplary POCIs and the substrate are shown in Fig. 5(c). Their intersectional lines are the grating lines whose tangential vector $\vec{\boldsymbol{g}}$ was already introduced above and which is given by

$$\vec{\boldsymbol{g}} = \vec{\boldsymbol{n}}_S \times \vec{\boldsymbol{k}}_{\boldsymbol{I}}. \tag{16}$$

Looking at the arrangement in direction of the grating vector $\vec{\boldsymbol{g}}$ as shown in Fig. 5(d) allows to identify the slant of the grating lines, given by the angle

$$\beta = \arccos\left(\frac{\vec{\boldsymbol{n}}_S \cdot \vec{\boldsymbol{k}}_{\boldsymbol{I}}}{|\vec{\boldsymbol{n}}_S| \cdot |\vec{\boldsymbol{k}}_{\boldsymbol{I}}|}\right) \tag{17}$$

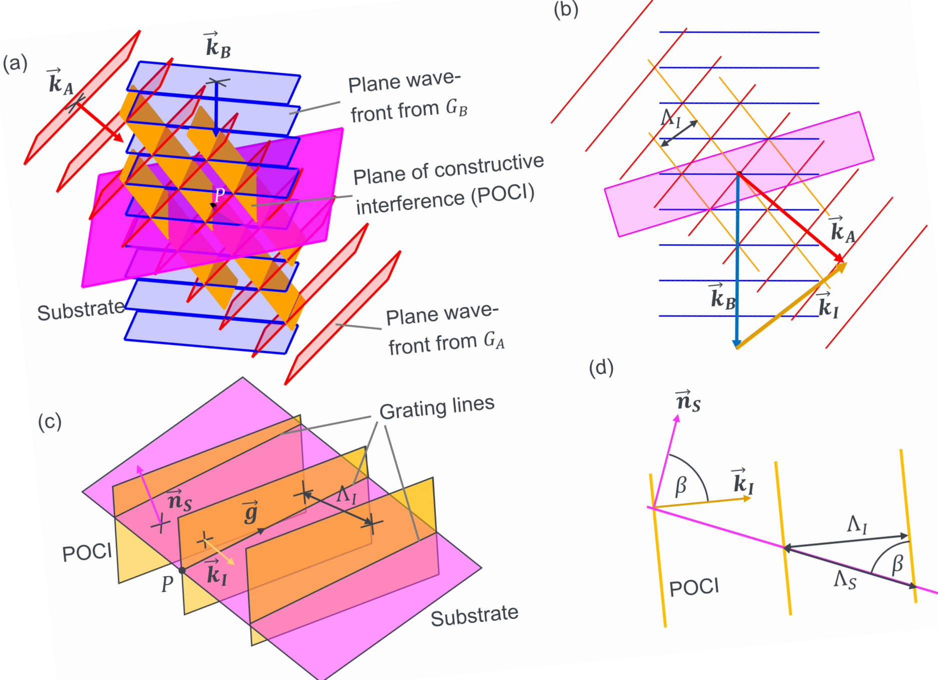


**Fig. 5.** Illustrations for the determination of the grating parameters at the point P. (a): Interference of the wavefronts of the two Gaussian beams on the substrate. The time-dependent wavefronts can be replaced by time-independent planes of constructive interference (POCIs). (b): Representation of the interference shown in (a) in a different orientation. (c): Derivation of the intersection lines, i.e. grating lines, from the POCIs and the substrate. (d): View of (c) in the direction along the tangential vector $\vec{g}$ of the grating lines.

between the POCIs and the substrate. The grating period $\Lambda_S$ resulting on the surface of the substrate finally is found to be

$$\Lambda_S = \frac{\Lambda_I}{\sin(\beta)}. \tag{18}$$

Combining this with Eq. (17) leads to

$$\Lambda_S = \frac{\Lambda_I}{\sin\left(\arccos\left(\frac{\vec{n}_S \cdot \vec{k}_I}{|\vec{n}_S| \cdot |\vec{k}_I|}\right)\right)}. \tag{19}$$

By replacing the numerator with Eqs. (14) and (15) and by rearranging the denominator using trigonometrical simplifications this yields

$$\Lambda_S = \frac{2\pi}{|\vec{k}_A - \vec{k}_B|} \cdot \left(1 - \left(\frac{\vec{n}_S \cdot (\vec{k}_A - \vec{k}_B)}{|\vec{n}_S| \cdot |\vec{k}_A - \vec{k}_B|}\right)^2\right)^{-\frac{1}{2}}. \tag{20}$$

The wave vector of the grating is given by

$$\vec{\Lambda}_S = \Lambda_S \cdot \frac{\vec{g} \times \vec{n}_S}{|\vec{g} \times \vec{n}_S|}. \tag{21}$$

The presented model allows for the calculation of the period, the inclination and the slant of the grating originating from the interference of arbitrarily orientated gaussian beams. Due to a

possible inhomogeneous overlap, caused by this arbitrary placement of the beams and due to their intrinsically inhomogeneous intensity distribution the contrast must be considered as well.

Although the formalism allows to calculate the three grating parameters for arbitrary points on the substrate's surface, without contrast (and also without intensity) they are meaningless. For this reason, a simple formalism of the intensity and the contrast is given in the following. For the sake of simplicity, it is assumed that the beams are perfectly coherent and ideally s-polarized. The average intensity at a point $P$ is simply defined as the sum of the intensities given as

$$I_{average} = I_A + I_B, \tag{22}$$

where $I_A$ is defined as

$$I_A = I_{0,A} \cdot e^{\frac{-r_P^2}{w_{00,A}^2(z_P)}} \tag{23}$$

with $I_0$ being the maximum intensity. $I_B$ is defined correspondingly. The values $z_P$ and $r_P$ are given by Eqs. (10) and (11). This definition of the intensity clearly neglects the interfering E-fields of the two beams. However, since no fixed phase relationship is defined between the two beams and since the intensity is considered on a macroscopic scale, this definition simplifies the calculation and is identical to the averaged intensity between multiple lines of the interference pattern around the point P. The contrast M is defined as [30]

$$M = \frac{2\sqrt{I_A/I_B}}{I_A/I_B + 1} \tag{24}$$

considering only the averaged intensities of the beams at the point $P$. When coherence, polarization, and pointing stability should be considered as well, the publication of Miller et. al. [30] is recommended, allowing for a simple extension of the presented model.

## 3. Simulation examples

Figure 6 shows an exemplary exposure configuration, simulated with a numerical code using the derived equations. Figure 6(a) shows the arrangement of the two Gaussian beams interfering on a wavy substrate, whose topography can be deducted from the color scale. The parameters of the beams and the surface function of the substrate are given in the description of the figure. Figure 6(b) and (c) show the spatial distribution of the grating period and the inclination of the grating lines (with respect to the vector [0 1 0]) on the substrate, indicated by the colormap. In Fig. 6(c) the additional black lines represent the grating vectors $\vec{g}$ at the corresponding points. The colormap in Fig. 6(d) shows the spatial distribution of the slant of the grating lines. Figure 6(e) and (f) show the calculated spatial distribution of the average intensity and the contrast.

Figure 7 shows the exemplary simulation of an exposure in classical LIL configuration. The parameters of the exposure are given in the description of the figure and the arrangement is the same as shown in [20]. This allows for a direct comparison between the point source model used in [20] and the gaussian model used in the present publication. When comparing the calculated distributions of the grating period and the inclination of the grating lines the high agreement between the two models becomes apparent when far-field exposure is considered.

Figure 8 shows the exemplary simulation of an exposure in SBIL configuration. The two beams are focused on a plane substrate and the parameters, which are given in the description of the figure, are based on the publication of Chen et al. [24]. The results of the simulation show that the SBIL still creates a period chirp, although it is very minor. When comparing the distribution of the inclination of the grating lines to the one arising from the LIL exposure (compare Fig. 8(b) with Fig. 7(b)) it becomes apparent that their sign is exactly opposite. This means that while the grating lines that arise from LIL incline away from the center (see also [20]), they incline towards the center in SBIL. This behavior can be explained using Fig. 1. While every point $P$ is

Optics EXPRESS

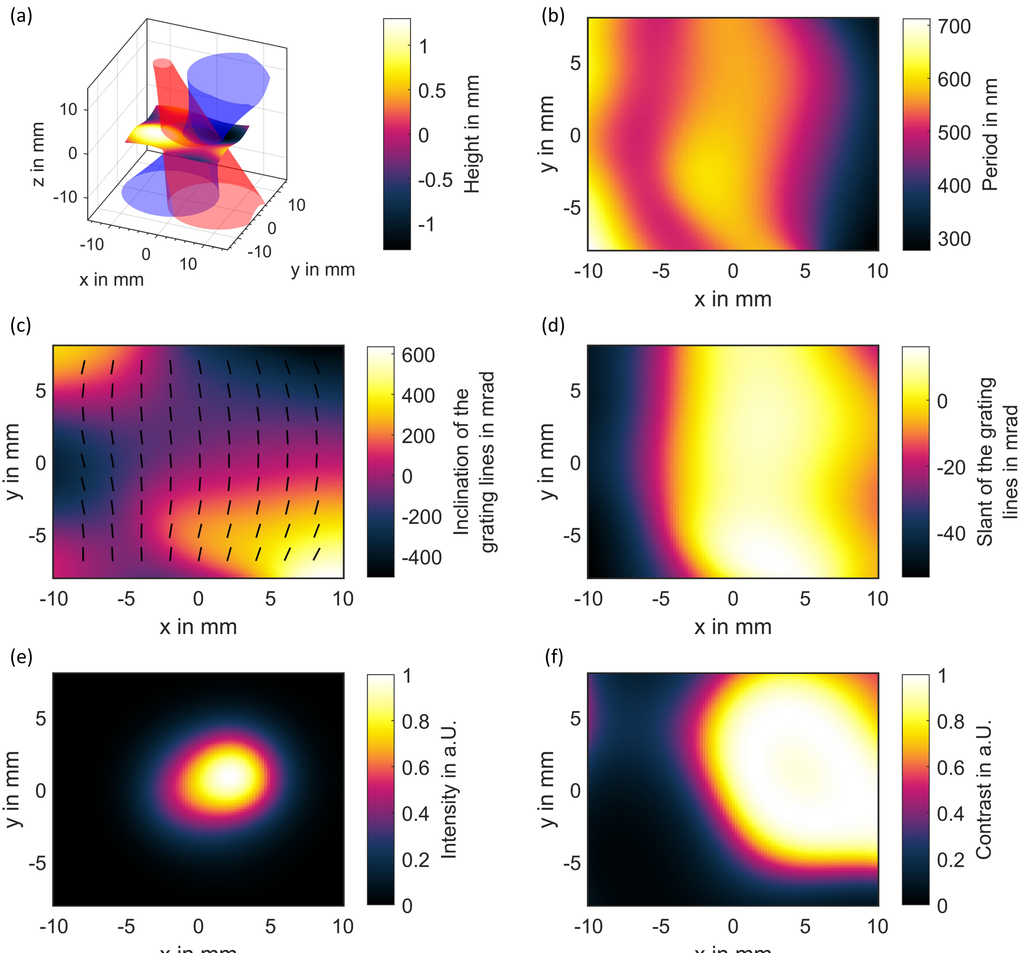


**Fig. 6.** Exemplary simulation of an arbitrary interference arrangement. (a): Geometrical arrangement showing the beams and a wavy substrate. The parameters of the beams are $z_{R,A}$ = 6 mm, $w_{00,A}$ = 1.5 mm, $z_{R,B}$ = 8 mm, $w_{00,B}$ = 4 mm. Their focuses are located at A = (6.8 mm, 0 mm, 18.8 mm) and B = (3 mm, 1 mm, 0.0001 mm), their wavelengths are $\lambda = 415$ nm and their directional vectors are $\vec{a}_A$ =[0.34 mm, 0 mm, -0.94 mm] and $\vec{a}_B$ =[-0.34 mm, 0 mm, -0.94 mm]. The function of the substate's surface is indicated by the color scale and given as $z(x, y) = -0.6 \cdot \sin(0.3 \cdot x) - 0.7 \cdot \sin(0.4 \cdot y)$. (b): Spatial distribution of the period. (c): Spatial distribution of the inclination of the grating lines between the grating vector $\vec{g}$ and the vector [0 1 0]. The black lines represent the grating vector $\vec{g}$. (d): Spatial distribution of the slant of the grating lines. (e): Spatial distribution of the intensity. (f): Spatial distribution of the contrast.

Optics EXPRESS

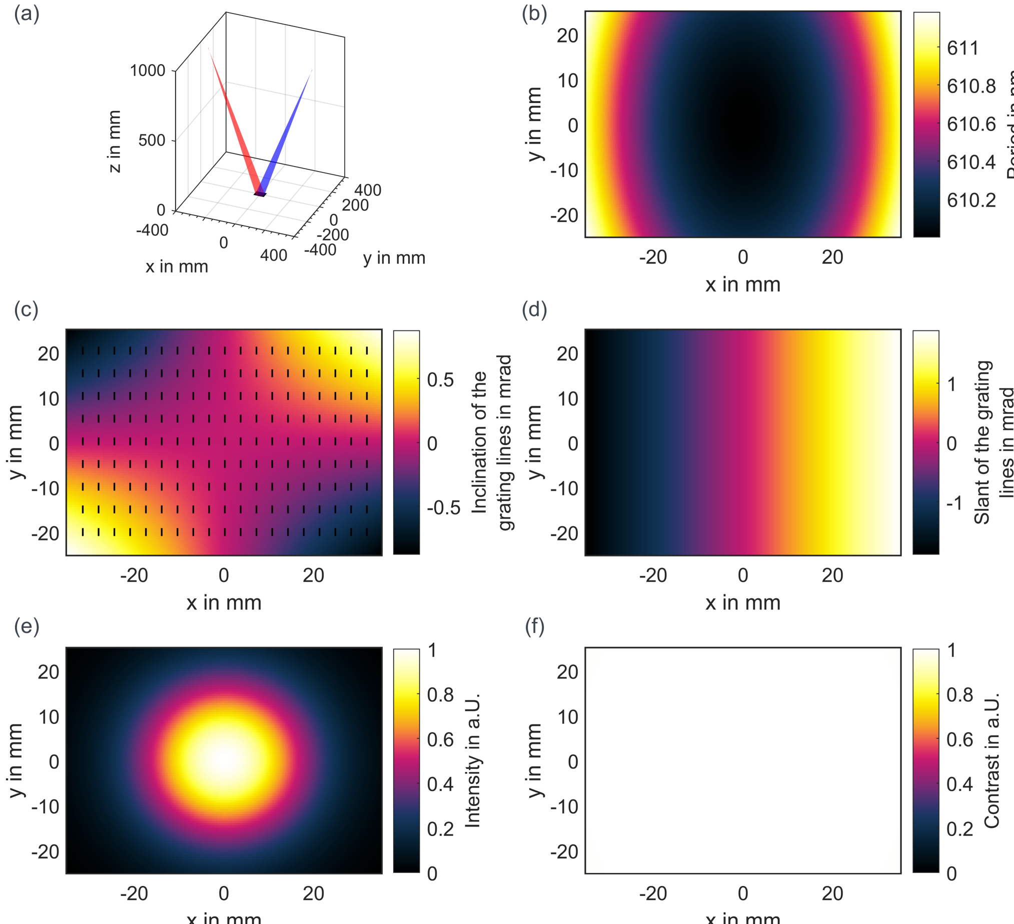


**Fig. 7.** Simulation of a LIL arrangement aiming for a period of $\Lambda_{aim} = 610$ nm on a plane substrate. Both beams are defined with $\lambda = 415$ nm, $z_R = 189.3$ µm and $w_{00} = 5$ µm. Their focuses are located at A = (-340.16 mm, 0 mm, 940.37 mm) and B = (340.16 mm, 0 mm, 940.37 mm) and their directional vectors are $\vec{a}_A$ =[-0.34 mm, 0 mm, -0.94 mm] and $\vec{a}_B$ =[-0.34 mm, 0 mm, -0.94 mm]. (a): Geometrical arrangement between the beams and the plane substrate located at z = 0 mm. (b): Spatial distribution of the period. (c): Spatial distribution of the inclination of the grating lines between the grating vector $\vec{g}$ and the vector [0 1 0]. The black lines represent the grating vector $\vec{g}$. (d): Spatial distribution of the slant of the grating lines. (e): Spatial distribution of the intensity. (f): Spatial distribution of the contrast.

exposed by two convex wavefronts in LIL (cf. Figure 1(a)), for SBIL every point $P$ experiences the interference between one concave and one convex wave (cf. Figure 1(b)), effectively making SBIL a type of the mixed interference case, cf. Reference [20].

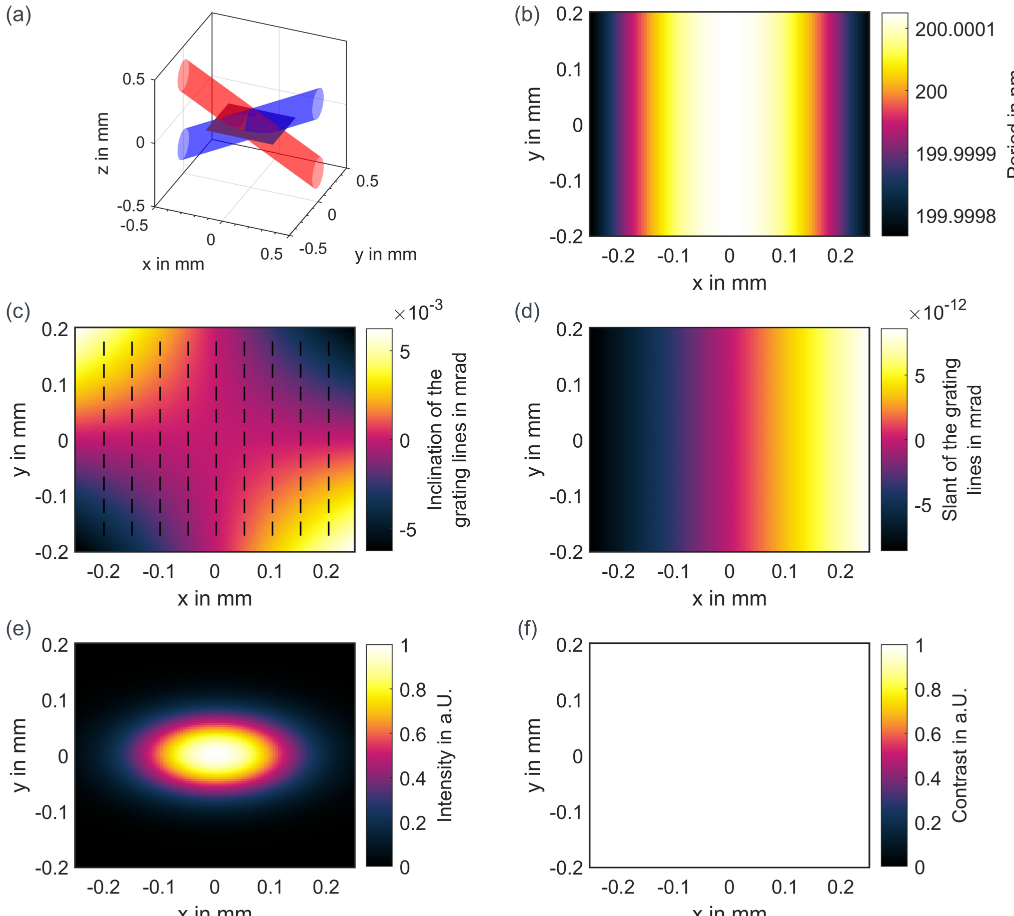


**Fig. 8.** Simulation of a SBIL arrangement presented in [24] aiming for a period of $\Lambda_{aim} = 200$ nm on a plane substrate. Both beams are defined with $\lambda = 351.1$ nm, $z_R = 89.48$ µm and $w_{00} = 0.1$ mm. Their focuses are located at A = (0 mm, 0 mm, 0 mm) and B = (0 mm, 0 mm, 0 mm) and their directional vectors are $\vec{a}_A$ =[0.88 mm, 0 mm, -0.48 mm] and $\vec{a}_B$ =[-0.88 mm, 0 mm, -0.48 mm]. (a): Geometrical arrangement between the beams and the plane substrate located at z = 0 mm. (b): Spatial distribution of the period. (c): Spatial distribution of the inclination of the grating lines between the grating vector $\vec{g}$ and the vector [0 1 0]. The black lines represent the grating vector $\vec{g}$. (d): Spatial distribution of the slant of the grating lines. (e): Spatial distribution of the intensity. (f): Spatial distribution of the contrast.

## 4. Conclusion

A general model for two-beam interference lithography was introduced unifying all possible cases of LIL without the need of adapting the mathematical equations to each case, as it is required for the typically used point source models [15–20]. Furthermore, it can also be used for the modelling of SBIL without any adaptations, which is presented here for the first time. The

Optics EXPRESS

interference of arbitrarily orientated and defined Gaussian beams on arbitrarily defined surfaces can be calculated with this model, while even the beam's gouy phase is respected. By defining two Gaussian beams by their position, direction, waist diameter, and Rayleigh length, equations were derived to determine their two wavefront vectors incident on a point $P$ on an arbitrarily shaped substrate. Further equations were derived enabling the determination of the grating period, the inclination of the grating lines, and the slant of the grating lines from these wavefront vectors. Finally, the given equations were implemented in code and three different exposure examples (i.e., an arbitrary, a LIL, and a SBIL arrangement) were calculated and presented.

**Funding.** InnovationsCampus Mobilität der Zukunft.

**Acknowledgments.** The authors would like to thank the Ministry of Science, Research and Arts of the Federal State of Baden-Württemberg for the financial support of the projects within the *InnovationsCampus Mobilität der Zukunft*.

**Disclosures.** The authors declare no conflicts of interest

**Data availability.** Data underlying the results presented in this paper are not publicly available at this time but may be obtained from the authors upon reasonable request.

## References

1. J. Qiao, A. Kalb, T. Nguyen, J. Bunkenburg, D. Canning, and J. H. Kelly, "Demonstration of large-aperture tiled-grating compressors for high-energy, petawatt-class, chirped-pulse amplification systems," Opt. Lett. **33**(15), 1684 (2008).
2. G. Andriukaitis, T. Balčiūnas, S. Ališauskas, A. Pugžlys, A. Baltuška, T. Popmintchev, M.-C. Chen, M. M. Murnane, and H. C. Kapteyn, "90 GW peak power few-cycle mid-infrared pulses from an optical parametric amplifier," Opt. Lett. **36**(15), 2755–2757 (2011).
3. C. Herkommer, P. Krötz, R. Jung, S. Klingebiel, C. Wandt, R. Bessing, P. Walch, T. Produit, K. Michel, D. Bauer, R. Kienberger, and T. Metzger, "Ultrafast thin-disk multipass amplifier with 720 mJ operating at kilohertz repetition rate for applications in atmospheric research," Opt. Express **28**(20), 30164–30173 (2020).
4. T. Wang, V. H. Nguyen, A. Buchenauer, U. Schnakenberg, and T. Taubner, "Surface enhanced infrared spectroscopy with gold strip gratings," Opt. Express **21**(7), 9005 (2013).
5. T. Kämpfe and O. Parriaux, "Depth-minimized, large period half-wave corrugation for linear to radial and azimuthal polarization transformation by grating-mode phase management," J. Opt. Soc. Am. A **28**(11), 2235 (2011).
6. G. Nordin and P. Deguzman, "Broadband form birefringent quarter-wave plate for the mid-infrared wavelength region," Opt. Express **5**(8), 163 (1999).
7. W. Yu, A. Mizutani, H. Kikuta, and T. Konishi, "Reduced wavelength-dependent quarter-wave plate fabricated by a multilayered subwavelength structure," Appl. Opt. **45**(12), 2601–2606 (2006).
8. M. Rumpel, M. Abdou Ahmed, A. Voss, and T. Graf, "Grating waveguide structures for intracavity generation of beams with azimuthal polarization in an Yb:YAG thin-disk laser," Laser Sources Appl. **8433**, 84331A (2012).
9. M. M. Vogel, M. Rumpel, B. Weichelt, A. Voss, M. Haefner, C. Pruss, W. Osten, M. Abdou Ahmed, and T. Graf, "Single-layer resonant-waveguide grating for polarization and wavelength selection in Yb:YAG thin-disk lasers," Opt. Express **20**(4), 4024–4031 (2012).
10. T. Dietrich, S. Piehler, M. Rumpel, P. Villeval, D. Lupinski, M. Abdou Ahmed, and T. Graf, "Highly-efficient continuous-wave intra-cavity frequency-doubled Yb:LuAG thin-disk laser with 1 kW of output power," Opt. Express **25**(5), 4917–4925 (2017).
11. T. Dietrich, S. Piehler, C. Rocker, M. Rumpel, M. Abdou Ahmed, and T. Graf, "Passive compensation of beam misalignment caused by air convection in thin-disk lasers," *2018 Conf. Lasers Electro-Optics, CLEO 2018 - Proc. 42*, 8–11 (2018).
12. M. Abdou Ahmed, M. Rumpel, A. Voss, and T. Graf, "Applications of sub-wavelength grating mirrors in high-power lasers," Adv. Opt. Technol. **1**(5), 381–388 (2012).
13. C. Lu and R. H. Lipson, "Interference lithography: A powerful tool for fabricating periodic structures," Laser Photonics Rev. **4**(4), 568–580 (2010).
14. C. J. M. Van Rijn, "Laser interference as a lithographic nanopatterning tool," J. Microlithogr. Microfabr. Microsystems **5**, 011012 (2006).
15. A. Katzir, A. C. Livanos, J. B. Shellan, and A. Yariv, "Chirped Gratings in Integrated Optics," IEEE J. Quantum Electron. **13**(4), 296–304 (1977).
16. K. Hibino and Z. S. Hegedus, "Hyperbolic holographic gratings: analysis and interferometric tests," Appl. Opt. **33**(13), 2553–2559 (1994).
17. H. Noda, T. Namioka, and M. Seya, "Geometric Theory of the Grating," J. Opt. Soc. Am. **64**(8), 1031–1036 (1974).
18. J. Ferrera, "Analysis of distortion in interferometric lithography," J. Vac. Sci. Technol. B **14**(6), 4009–4013 (1996).
19. H. Kim, H. Jung, D.-H. Lee, K. B. Lee, and H. Jeon, "Period-chirped gratings fabricated by laser interference lithography with a concave Lloyd's mirror," Appl. Opt. **55**(2), 354–359 (2016).

Optics EXPRESS


20. F. Bienert, T. Graf, and M. Abdou Ahmed, "Comprehensive theoretical analysis of the period chirp in laser interference lithography," Appl. Opt. **61**(9), 2313–2326 (2022).
21. F. Bienert, T. Graf, and M. Abdou Ahmed, "Theoretical investigation on the elimination of the period chirp by deliberate substrate deformations," Opt. Express **30**(13), 22410 (2022).
22. M. E. Walsh and H. I. Smith, "Method for reducing hyperbolic phase in interference lithography," J. Vac. Sci. Technol. B **19**(6), 2347–2352 (2001).
23. C. G. Chen and M. L. Schattenburg, "A brief history of gratings and the making of the MIT Nanoruler," J. Vac. Sci. Technol., 1–10 (2004).
24. C. G. Chen, P. T. Konkola, R. K. Heilmann, C. Joo, and M. L. Schattenburg, "Nanometer-accurate grating fabrication with scanning beam interference lithography," Nano- Microtechnology Mater. Process. Packag. Syst. **4936**, 126–134 (2002).
25. P. T. Konkola, C. G. Chen, R. K. Heilmann, C. Joo, J. C. Montoya, C.-H. Chang, and M. L. Schattenburg, "Nanometer-level repeatable metrology using the Nanoruler," J. Vac. Sci. Technol. B **21**(6), 3097–3101 (2003).
26. T. Graf, *Laser* (Vieweg + Teubner Verlag, 2009).
27. Rüdiger Paschotta, "The Gouy Phase Shift Speeds up Light - The Photonics Spotlight," https://www.rp-photonics.com/spotlight_2008_11_25.html.
28. Y. Shen, T. Liu, Q. Zhu, J. Wang, and C. Jin, "Dislocated Double-Layered Metal Gratings: Refractive Index Sensors with High Figure of Merit," Plasmonics **10**(6), 1489–1497 (2015).
29. M. E. Walsh, "On the design of lithographic interferometers and their application," 1–300 (2004).
30. D. B. Miller, A. Jones, and R. R. McLeod, "Contrast analysis in two-beam laser interference lithography," Appl. Opt. **59**(18), 5399 (2020).


129.69.140.76 {ts '2024-08-06 11:51:09'}